Short-timescale X-ray spectral variability in the Seyfert 1 galaxy NGC 3783

Costanzo, D.; Dadina, M.; Vignali, C.; De Marco, B.; Cappi, M.; Petrucci, P.O.; ... ; Matzeu, G.A.

A&A 659, A161 (2022)
https://doi.org/10.1051/0004-6361/202142279

Astronomy & Astrophysics

Short-timescale X-ray spectral variability in the Seyfert 1 galaxy NGC 3783

D. Costanzo[1,2], M. Dadina[2], C. Vignali[1,2], B. De Marco[3], M. Cappi[2], P. O. Petrucci[4], S. Bianchi[5], G. A. Kriss[6], J. S. Kaastra[7,8], M. Mehdipour[6,7], E. Behar[9], and G. A. Matzeu[1,2]

[1] Dipartimento di Fisica e Astronomia "Augusto Righi", Università degli Studi di Bologna, Via Gobetti 93/2, 40129 Bologna, Italy
e-mail: deborah.costanzo2@unibo.it
[2] INAF – Osservatorio di Astrofisica e Scienza dello Spazio di Bologna, Via Gobetti 93/3, 40129 Bologna, Italy
[3] Departament de Física, EEBE, Universitat Politecnica de Catalunya, Av. Eduard Maristany 16, 08019 Barcelona, Spain
[4] Univ. Grenoble Alpes, CNRS, IPAG, 38000 Grenoble, France
[5] Dipartimento di Matematica e Fisica, Università degli Studi Roma Tre, via della Vasca Navale 84, 00146 Roma, Italy
[6] Space Telescope Science Institute, 3700 San Martin Drive, Baltimore, MD 21218, USA
[7] SRON Netherlands Institute for Space Research, Niels Bohrweg 4, 2333 CA Leiden, The Netherlands
[8] Leiden Observatory, Leiden University, PO Box 9513, 2300 RA Leiden, The Netherlands
[9] Department of Physics, Technion, Haifa 32000, Israel

Received 22 September 2021 / Accepted 16 December 2021

ABSTRACT

Aims. We report on the X-ray time-resolved spectral analysis of *XMM-Newton* observations of NGC 3783. Our main goal is to detect transient features in the Fe K line complex in order to study the dynamics of the innermost accretion flow.
Methods. We reanalyse archival observations of NGC 3783, a bright local active galactic nucleus, for which a transient Fe line was reported, complementing this data set with new available observations. This results in a long set of observations which can allow us to better assess the significance of transient features and possibly test their recurrence time. Moreover, as the new data catch the source in an obscured state, this analysis allows also to test whether the appearance and disappearance of transient features is linked to the presence of obscuring gas.
Results. We detect discrete features at the ≥90% significance level both in emission and in absorption at different times of the observations, split into 5 ks time-resolved spectra. The overall significance of individual features is higher in the obscured dataset. The energy distribution of the detections changes between the two states of the source, and the features appear to cluster at different energies. Counting the occurrences of emission and absorption lines at the same energies, we identify several groups of $\geq 3\sigma$ detections: emission features in the 4–6 keV band are present in all observations and are most likely due to effects of the absorber present in the source; an emission line blend of neutral Fe Kβ and ionised Fe Kα is present in the unobscured dataset; absorption lines produced by gas at different outflowing velocities and ionisation states show an increase in energy between the two epochs, shifting from ∼6.6 keV to ∼6.7–6.9 keV. The representation of the features in a time–energy plane via residual maps highlights a possible modulation of the Fe Kα line intensity linked to the clumpiness of the absorbing medium.

Key words. galaxies: individual: NGC 3783 – galaxies: Seyfert – X-rays: galaxies – galaxies: active

1. Introduction

Active galactic nuclei (AGN) show variability at any wavelength over a wide range of timescales, from minutes to years (e.g. Padovani et al. 2017). In the X-ray band, variability is found to be much faster than in other wavelengths; this is ascribed to variable phenomena happening in the innermost regions of the accretion flow (corona and inner disc), that is, at a few tens of gravitational radii ($R_g = GM/c^2$) from the supermassive black hole (SMBH; e.g. Mushotzky et al. 1993). Moreover, these same variable phenomena may drive (at least part of) the variability from the outer accretion disc which is observed at longer wavelengths (UV and optical) and over longer timescales (Kotov et al. 2001; Arévalo & Uttley 2006). Observing diverse timescales for variability in distinct parts of the spectrum can help us to distinguish the different processes in action and understand where they are possibly originating.

Seyfert 1 galaxies are the best targets with which to study these regions because they are the brightest in X-rays and are thought to be observed 'face-on' from an angle of typically ≤30°, that is, with a clear and direct view of the accretion flow (Urry & Padovani 1995). Their X-ray spectra show many emission features, the most prominent being the fluorescent neutral Fe Kα line at 6.4 keV. This line likely originates from the reflection of the primary continuum on the accretion disc. We expect that its shape and energy are altered by the proximity to the SMBH (Fabian et al. 2000) and/or by the geometry and physical state of the accretion flow. Absorption features can also be present, suggesting the presence of outflows (winds) along the line of sight; their dynamics and changes in their physical state (e.g. density and ionisation) can be traced by studying absorption-line variability (Pounds et al. 2003; Reeves et al. 2003; Dadina et al. 2005; Tombesi et al. 2010). While variability patterns have been intensively studied for emission lines (e.g. Iwasawa et al. 2004; De Marco et al. 2009), analysis of variable absorption features is generally more challenging. Nevertheless, this latter holds the potential to unveil the location of winds. Moreover, a simultaneous study of emission and absorption

Article published by EDP Sciences

variability could highlight possible correlations between accretion and ejection phenomena that could deepen our understanding of the launching mechanism for outflows.

The goal of this study is a systematic and simultaneous time-resolved spectral analysis of emission/absorption features in the spectra of an X-ray bright Seyfert galaxy, NGC 3783. This source presents interesting properties for the study of variable emission and absorption lines, as detailed below, and is one of brightest with long *XMM-Newton* EPIC/pn observations. Some of these observations, namely those taken in 2000 and 2001, have already been analysed with time-resolved spectral analysis (Tombesi et al. 2007; De Marco et al. 2009), focusing on the variability properties of the emission features. We add a characterisation of the absorption lines present in those same datasets and analyse new observations taken in 2016. This allows us to also study the variations of the emission and absorption lines on long timescales.

NGC 3783 is a Seyfert 1 galaxy at redshift $z = 0.0097$ (Theureau et al. 1998) with a SMBH mass of $M = 3.0 \pm 0.5 \times 10^7\,M_\odot$, as estimated via reverberation mapping studies in optical and *UV* bands (Peterson et al. 2004). Analysing the *XMM-Newton* observation taken in 2001, Reeves et al. (2004, hereafter R04) identified several features: a strong Fe Kα at 6.4 keV, an emission line at ∼7 keV due to a blend of neutral Fe Kβ and H-like Fe, and absorption at ∼6.6 keV due to highly ionised Fe, plus an absorption edge at ∼7.1 keV. In the same dataset, Tombesi et al. (2007) found a modulation of the flux and a correlated variation of the Fe Kα with a broad redshifted component on timescales of ∼27 ks. In December 2016, during a *Swift*/XRT monitoring program, NGC 3783 showed heavy X-ray absorption produced by an obscuring outflowing gas (Mehdipour et al. 2017, M17 hereinafter). As a result, new absorption lines from Fe XXV and Fe XXVI appeared in the *XMM-Newton* spectrum. From their analysis of the outflow, M17 found a column density of a few $10^{23}\,\mathrm{cm}^{-2}$ and a velocity of a few thousand $\mathrm{km\,s}^{-1}$ and interpreted it as a clumpy, inhomogeneous medium consistent with clouds at the base of a radiatively driven disc wind located in the outer broad line region of the AGN. A similar but less intense obscuration event was revealed by Kaastra et al. (2018) in a *Chandra*/HETG observation taken in August 2016, with a column density of one order of magnitude lower than that derived in December 2016. Using all the X-ray observations of NGC 3783, from 1993 (ASCA) to 2016 (*Chandra*), it was clear that the source displayed an absorption column density larger than $10^{22}\,\mathrm{cm}^{-2}$ in roughly 50% of the observing time. De Marco et al. (2020, hereafter DM20), constrained the short-timescale (from about one hour to ten hours) variability properties of the obscurer in the 2016 *XMM-Newton* dataset. Their spectral-timing analysis showed that the observed fast variations in the soft X-rays were consistent with changes in the ionisation parameter. This study allowed a recombination time of $\lesssim$1.5 ks to be inferred, corresponding to a lower limit on the electron density of $n_e \sim 7.1 \times 10^7\,\mathrm{cm}^{-3}$. This value is consistent with the results of M17 and places the obscurer at a distance of between 7 and 10 light days.

Here, we present the results from the overall *XMM-Newton* available datasets. We present a comprehensive and detailed time-resolved spectral analysis, the aim of which is to detect variable line-like features, either in emission or in absorption (Sect. 3). The statistical significance of the analysis is then estimated in Sect. 3.4 using detailed Monte Carlo simulations. Non-random patterns of variability are searched for (Sect. 4) and overall findings are then discussed (Sect. 5).

Table 1. Log of the *XMM-Newton* observation of NGC 3783 used in this work.

	Obs ID	Start date DD/MM/YYYY	Flux	Exposure ks
U1	0112210101	28/12/2000	3.91	26
U2	0112210201	17/12/2001	3.13	87
U3	0112210501	19/12/2001	4.06	87
O1	0780860901	11/12/2016	2.11	76
O2	0780861001	21/12/2016	2.54	38

Notes. The columns report: (1) the nomenclature used throughout the paper to refer to each observation; 3) the observation ID; 3) the observation date; 4) the 4.5–10 keV flux (in units of 10^{-11} erg s^{-1} cm^{-2}) taken from 4XMM-DR10 catalogue (Webb et al. 2020); 5) the effective exposure (after removal of flares). We note that observation U2 is split in two parts (U2a and U2b, of 40 ks and 47 ks respectively), separated by ∼4 ks.

2. *XMM-Newton* observations and data reduction

There are seven observations of NGC 3783 in the *XMM-Newton* Science Archive, but two of them (OBS ID 0112210401 and OBS ID 0112210601) were excluded from our analysis because of their short duration (∼4 ks). The remaining observations we analysed are listed in Table 1. Following M17 and DM20, we identify two epochs, corresponding to the state of the source: observations from 2000 and 2001 caught the source in an unobscured state, and are hereafter identified as U1, U2, and U3, while during the observations taken in 2016 the source was in an obscured state, and so these are named O1 and O2.

We used data from the EPIC pn detector only, because of its higher effective area with respect to the MOS. The camera was operated in Small Window mode during all observations. Data were reduced using the XMM-SAS v.16.1 following standard procedures. Running the `epproc` task resulted in U2 being split into two parts (U2a and U2b) separated by ∼4 ks. Source photons were collected from circular regions of 45 arcsec radius, while background photons were extracted from an offset circle of 65 arcsec radius close to NGC 3783 and free of any background sources. Observations U1, U2, and U3 show limited or no high-background intervals, which were present only at the end of the pointing. Observations O1 and O2 were affected by several flares, which were removed by imposing a threshold in the count rate at 0.2 cts s^{-1} for energies >10 keV. The resulting exposure time of the cleaned event files are reported in Table 1. The background-subtracted light curves were obtained with the SAS routine `epiclccorr` and are shown in Fig. 1. Using the `epatplot` task, we verified the absence of pile-up. Response matrices were produced with the SAS tasks `arfgen` and `rmfgen`, and spectra were analysed using the XSPEC v.12.9 software package (Arnaud et al. 1996).

3. Variable features search

In order to probe the closest regions to the SMBH, we need to sample the shortest possible variability timescales. On these timescales, transient and variable emission and absorption features may manifest. These can, for example, be due to the variability of the primary irradiating X-ray continuum or to motions of the outflowing gas. To study these features, we relied on time-resolved spectral analysis techniques. The aim of our approach is to eventually find features that would not be detected in average spectra: because of their transient or variable nature, they could

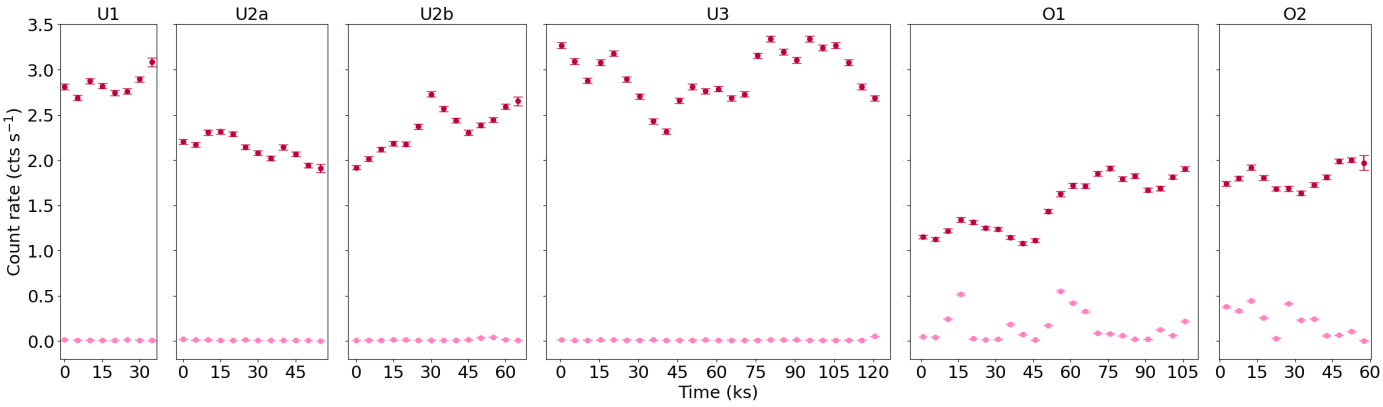

Fig. 1. Background-subtracted light curve of NGC 3783 (red points) with the corresponding background (pink points) extracted in the 4–10 keV band. The time bins are 5 ks. The identifiers of each observation (U1-3, O1-2) refer to the state of the source (Unobscured, Obscured), as described in Sect. 2.

be averaged out over long exposure times. Nevertheless, there is an observational limit to the proximity to the SMBH (and minimum timescale) which is set by the photon count-rate available. Therefore, the time resolution of our spectra corresponds to a trade off between sampling short timescales and retaining a sufficient number of counts within each time-resolved spectrum to allow for a meaningful statistical analysis. In order to identify the physical scales that we can probe, we first considered the Keplerian orbital period at a given distance (in R_g) from a black hole with adimensional spin a (Bardeen et al. 1972):

$$t = 310 \left[a + \left(\frac{R}{R_g} \right)^{\frac{3}{2}} \right] M_7 \ (s). \tag{1}$$

Given the BH mass of NGC 3783 of $3 \times 10^7 \, M_\odot$ (Peterson et al. 2004) and using a spin value $a = 0$, we find that a time resolution of 5 ks corresponds to the orbital period at $\sim 3 \, R_g$. This carries the potential to over-sample periodicities or non-random variations occurring at larger radii, meaning that we may probe and map regions just outside of the event horizon. We note that, in terms of light travel time, 5 ks corresponds to a few tens (~35) of R_g. We then verified that using this duration as a time resolution allows us to have good photon statistics. To this aim, we extracted spectra in time bins of 5 ks; to give an idea of the available number of counts, the spectrum with the lowest flux (ninth bin of O1) provides ~3500 photons in the 4–10 keV band. By assuming this time resolution, we obtain a total of 88 spectra, namely 56 for the unobscured dataset and 32 for the obscured one.

3.1. Baseline model

We first chose a baseline model for each time-resolved spectrum to describe the broad-band continuum. Focusing on the 4–10 keV energy band allows us to apply a simple model that only includes a power law, an absorption component (intrinsic to the source, as the Galactic absorption does not have effects at these energies), and a narrow Gaussian emission line for the neutral Fe Kα line. A combination of cold, mildly ionised, and partial covering absorbers has been detected in this source (R04, Yaqoob et al. 2005, M17, Mao et al. 2019); these absorbers were particularly intense during the obscured observations (M17)[1]. However, the duration of our time slices prevents us from testing such complex scenarios. To embrace at least one of the aspects that is common to all of the absorption schemes presented in the literature, we decided to adopt a partial covering model due to cold matter. This, in principle, should allow the fitting to mimic, if necessary, smoothed curvatures due to either ionised or cold absorbers. On the one hand, far from being a totally realistic representation of what is really happening in the source, our choice is meant to reduce any systematic errors due to an extremely oversimplified modelling of the continuum by as much as possible, at the cost of one single degree of freedom. On the other hand, as our choice intrinsically includes the possibility of having a total obscurer, it is consistent with works where similar techniques were adopted (Tombesi et al. 2010; Gofford et al. 2013). Moreover, models of ionised gas were not chosen here because they typically include discrete absorption features, i.e. those that we aim to study separately and individually. As for the iron line, in NGC 3783 this feature is known to be present (R04, Tombesi et al. 2007, M17, DM20) and is typically sufficiently strong (EW ~ 100–150 eV) to alter the 4–10 keV continuum fit if not properly taken into account. We define this as our baseline model, i.e. in XSPEC terminology `pcfabs` × `(power law + gauss)`.

3.2. Fe Kα line

Following the results of M17, we assume the Fe Kα to be narrow, with a frozen width of 10 eV. The other line parameters (energy and normalisation) are left free to vary.

In Fig. 2 we show the energy, normalisation, and equivalent width (EW) of the narrow Fe Kα as obtained from the fits of each time-resolved spectrum, and their average values in individual observations. We do not observe major variability in the line parameters, apart from a shift in the centroid energy (~50 eV) between unobscured and obscured data. We checked if a similar behaviour is also measurable in the MOS data using the average spectra for each of the five observations, but we do not find any evidence for such a shift. We therefore conclude that the observed shift is most probably due to

[1] We note that multi-layers of partially covering obscurers at mild-to-neutral ionisation state have been extensively found in Seyfert 1 galaxies in the last decade (e.g. Turner et al. 2009; Longinotti et al. 2009; Reeves et al. 2014; Kaastra et al. 2014; Cappi et al. 2016). These absorbers are in addition to the multi-component warm absorbers which are typically total covering and highly ionised (Blustin et al. 2005; Piconcelli et al. 2005; McKernan et al. 2007; Laha et al. 2014).

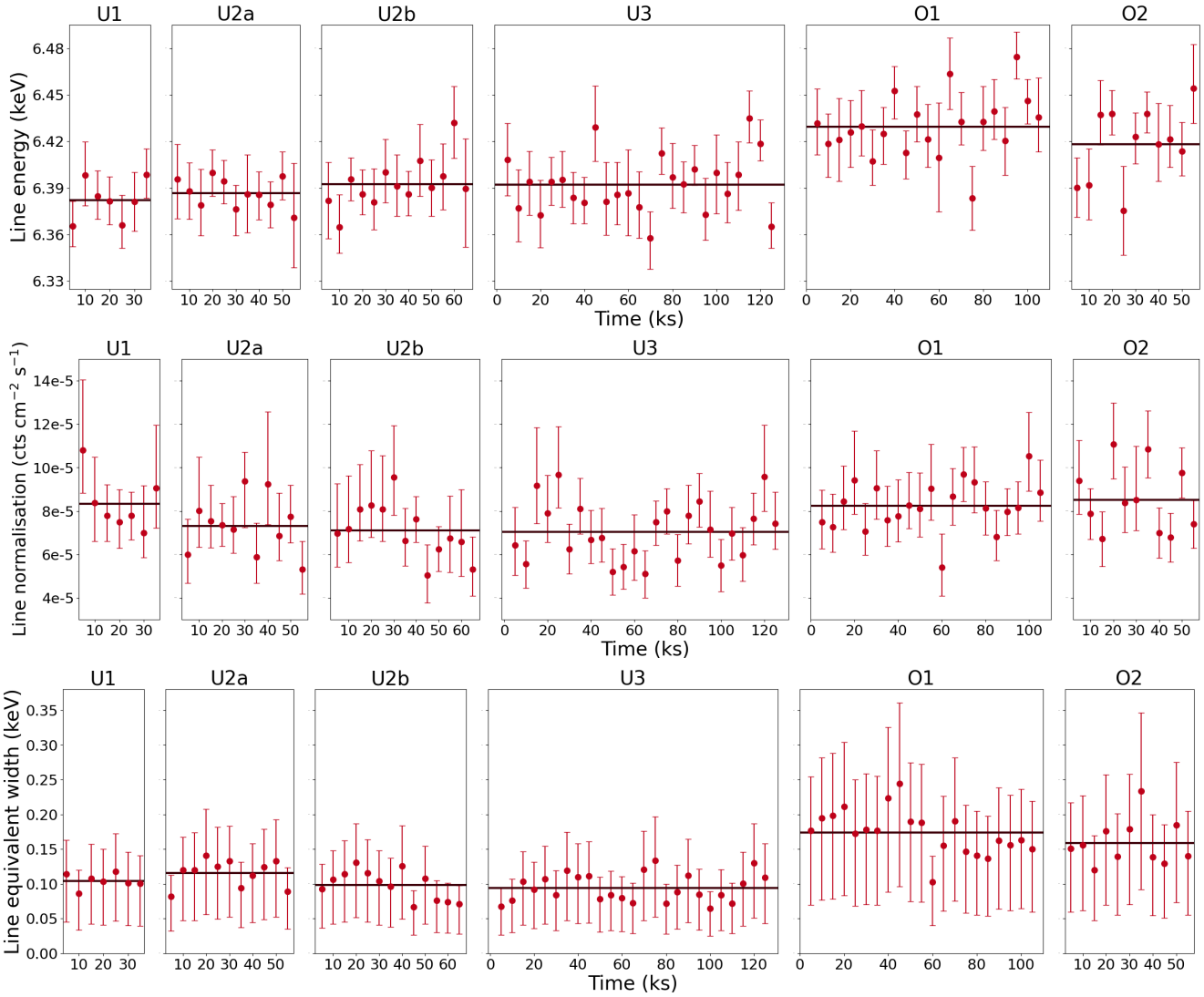

Fig. 2. Rest-frame energy (*top panel*), normalisation (*middle panel*), and EW (*bottom panel*) of the narrow Fe Kα line included in the baseline model; errors are reported at 1σ.

uncorrected charge-transfer-inefficiency (CTI) evolution that translates into a poor gain calibration, as described in Ponti et al. (2013), Mehdipour et al. (2015), and Zoghbi et al. (2019). In addition, the energy of the narrow Fe K line displays some short episodes of significant variation (see U3, O1, and O2 in the upper panels of Fig. 2) on timescales of tens of kiloseconds.

Interestingly, the line EW seems to be constant within each single pointing, despite the almost 30% variability in continuum flux for the most extreme cases (Fig. 1, U2b, U3, O1). This is not expected if we assume that the narrow Fe Kα emission line is produced far from the origin of the primary X-rays. In this case, we would expect a decoupling between the two quantities due to the time delays introduced by the distance of the reprocessor. The easiest way to explain what is presented in the lower row of Fig. 2 is to associate this emission component with a feature produced in the vicinity (i.e. fast responding) of the SMBH. Under this assumption, one would expect it to be related to the relativistically modified iron emission line. On the one hand, if this were the case, we would expect some variability in line shape on short timescales, as predicted for example in light-bending scenarios (Miniutti & Fabian 2004); on the other hand, D20 demonstrated that the variability of the source is also strongly influenced by changes in the absorber characteristics on short timescales (~1500 s). This is in agreement with the apparent steadiness of the EW of the emission feature. Overall, we stress here that the 1σ error on the Fe Kα line normalisation is of the order of 25% − 30% (middle row of Fig. 2). This heavily impacts our capability to deeply investigate the iron line intensity variability on these timescales. We cannot claim strong evidence for variation, but at the same time we cannot exclude them if they are of the order of ~10%.

On longer timescales, from 2001 to 2016 observations, an increase can be seen in the average value of Fe Kα EW of the order of 70 eV. Assuming that the energy of the line remains the same between the two sets of observations, this increase in EW is consistent with the rise of the absorber column density and decrease in flux (M17).

We then verified whether the assumption of a narrow line (width fixed at 10 eV) was correct, and let its width free to vary. We obtained average values of its width of ~30 eV for the unobscured state and ~70 eV for the obscured state (Fig. 3). However, the width was always consistent with zero to within 2 σ. We therefore decided to keep the width frozen to 10 eV for the following steps of the analysis.

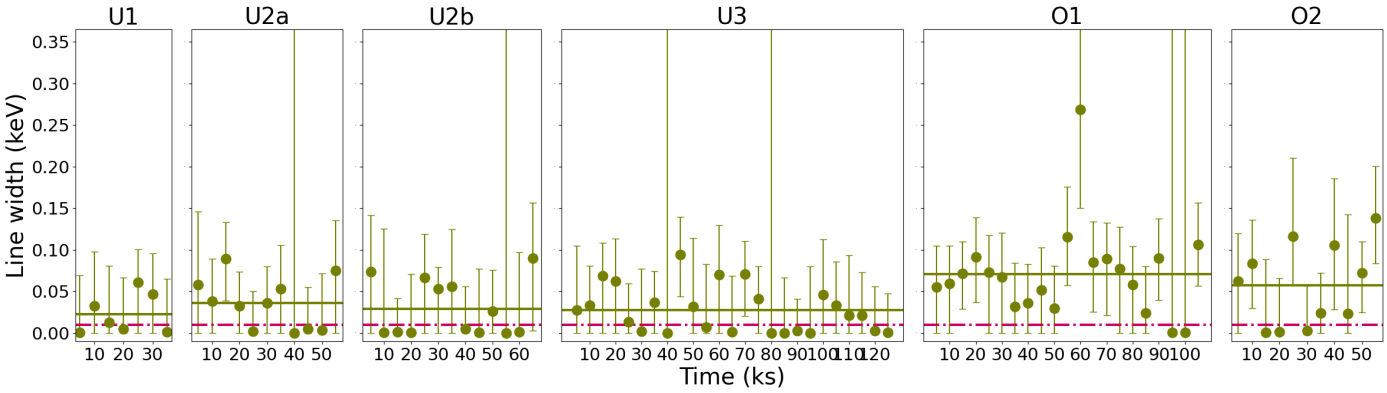

Fig. 3. Width of the Fe Kα line. The magenta dotted line marks the frozen 10 eV width used in the baseline model. All errors are reported at 1σ.

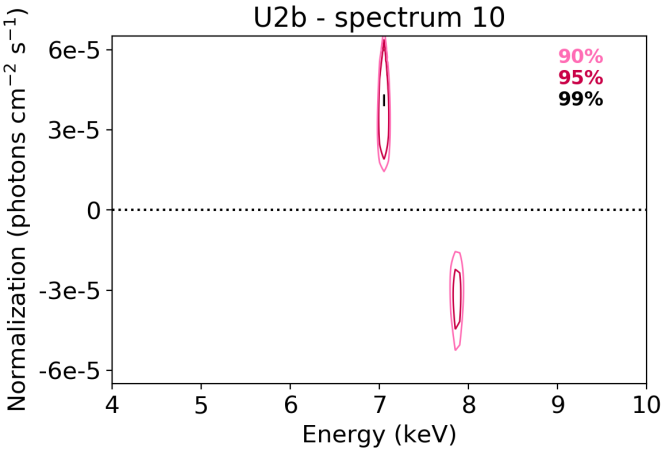

Fig. 4. An example of the significance contours found with the blind search in a single 5 ks spectrum. An emission line is detected at $\sim 3\sigma$ (99%, i.e. $\Delta\chi^2 \leq -11.34$, Δd.o.f. = 3) at $\sim$6.9 keV and an absorption line is detected at $\sim 2\sigma$ (95%, i.e. $-7.81 \geq \Delta\chi^2 > -11.34$, Δd.o.f. = 3) at $\sim$7.9 keV.

3.3. Blind search

After fitting the baseline model described in Sect. 3.1, we carry out a blind search for additional emission and absorption features. As the only discrete component present in the baseline model is the Fe Kα, we may expect to also detect features (like the Fe Kβ/ionised Fe Kα blend and the absorption lines described in R04 and M17) that appear in the average spectrum. Our purpose is to verify whether they are present at all times or rather show some variation. We apply a procedure similar to that adopted in Tombesi et al. (2010): a second Gaussian component is included in the model, allowing for both positive and negative values of the normalisation, and with width in the range 0.01–0.5 keV. Then the `steppar` command is launched simultaneously on the line energy parameter (which can vary from 4 to 10 keV, with increments of 5 eV) and the normalisation parameter (from -6.5 to $+6.5 \times 10^{-5}$ photons s^{-1} cm^{-3}, with increments of 6.5×10^{-7} photons s^{-1} cm^{-3}). We then plot the significance contours corresponding to $\Delta\chi^2$ of -6.25, -7.81, and -11.34, which for three free parameters represent a significance of the line of 1.6 ($\leq$90%), 2 ($\leq$95%), and 3 ($\leq$99%) σ, respectively. An example of these contour plots is shown in Fig. 4, where an emission line is detected at $\sim 3\sigma$ at E $\sim$ 6.9 keV and an absorption line is found at $\sim 2\sigma$ at $\sim$7.9 keV.

This procedure is repeated for all the 5 ks time-resolved spectra. As the obscuration state of the X-ray source may influence the number and type (i.e. emission vs absorption) of lines, we analysed the features detected in the two states separately.

Figure 5 reports the distributions of the detected emission and absorption features as a function of their observed-frame energy. The vertical dotted line represents the nominal energy of the Fe Kα emission and is shown only as a visual reference, because in the current analysis this feature is already included in the model as a narrow emission line (see Sect. 3.2). The occurrences of the features are normalised to the number of analysed spectra, that is, 56 for the unobscured case and 32 for the obscured case. Interestingly, the energy of the detected emission and absorption lines seems to cluster around certain values. Starting with the emission lines, in the unobscured data we recognise a small peak in the distribution (corresponding to a total of eight detections in time-resolved spectra) at the energy of the Kβ/ionised Kα line, corresponding to the Kβ/ionised Kα blend. In the obscured state (Fig. 5, bottom-left), most of the detected lines are clustered between $\sim$5.6 keV and $\sim$6.4 keV.

For the absorption features, most of the detections cluster between $\sim$6.4 keV and $\sim$7 keV. While no major difference is observed in the distribution of clustered features in unobscured and obscured observations, there seems to be a slight shift towards higher energies in the obscured datasets.

3.4. Simulations and significance of the features

To assess the statistical significance of the individual lines, we followed the indications reported by Protassov et al. (2002) and Vaughan & Uttley (2008). In particular, after a preliminary assessment in which we evaluated the $\Delta\chi^2$ for the 3 Δd.o.f. of the detected line (energy, normalisation, width), we used Monte Carlo techniques to compute the number of times a line at a given energy and significance is found by chance in simulated, featureless spectra. In doing so, we took advantage of what we found in real data: the detected features we are looking for in the simulations do not appear to be random fluctuations, that can be positive or negative, but lines clustered in determined regions of the spectrum that are bound to be strictly positive or negative. We therefore tested separately emission and absorption lines.

To probe the different source states, we analysed the unobscured and obscured epochs separately, because of their intrinsic diversity, and for each epoch we made a selection in X-ray flux, identifying low-, medium-, and high-flux states. For the 2000/2001 datasets, the flux ranges are 2.50–3.09, 3.09–3.68, and 3.68–4.27 $\times$ 10^{-11} erg s^{-1} cm^{-2}, while for the

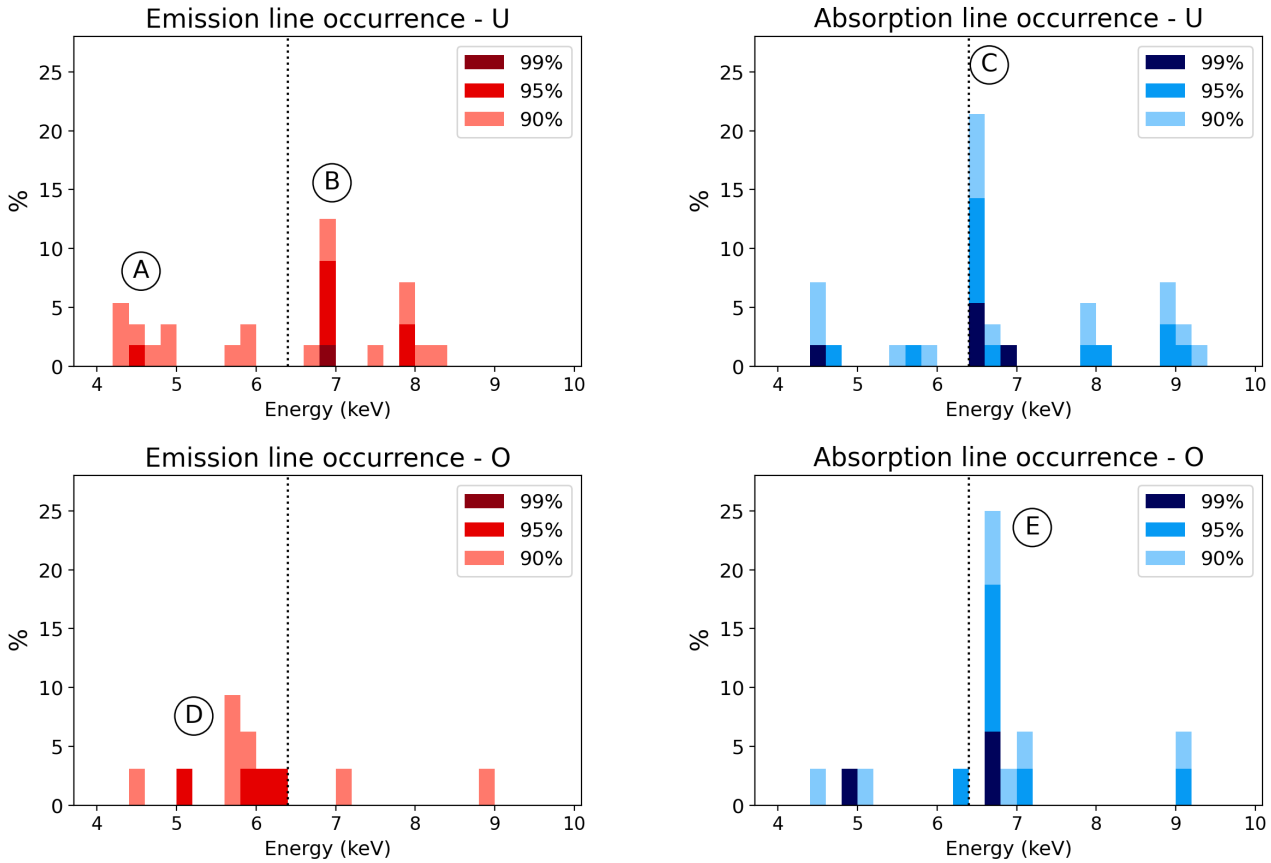

Fig. 5. Distribution in energy (observed frame) of the features detected via blind search. The energy bins are 0.2 keV wide. *Top panels*: results of the unobscured dataset (U1, U2a, U2b, U3), while the *bottom panels* refer to the obscured datasets (O1, O2). *Left panels*: detections of emission lines are reported (red), while the *right panels* report detections of absorption lines (blue): in both cases, the darker the colour the higher the significance, i.e. the measured $\Delta\chi^2$. The percentage on the y axes is the ratio between the number of detections in each bin and the total number of spectra for the two sets of observations (56 in total for the unobscured, and 32 in total for the obscured). The dotted line reported in all four figures is the nominal energy of the Fe Kα and is shown purely as a visual reference. The letters A–E indicate the clusters of lines that globally reach a significance $\gtrsim 3\sigma$, as indicated in Table 2 and described in Sect. 3.4.

2016 dataset the three flux intervals are 1.42−1.80, 1.80−2.19, and $2.19-2.57\times10^{-11}$ erg s^{-1} cm^{-2}, respectively. We determined a best-fit baseline model (using the same continuum model defined in Sect. 3.1) for each of these groups of spectra (six in total), and used it to simulate 1000 spectra for each group. Simulated spectra are grouped at one-fifth of the instrument energy resolution. We first apply and fit the baseline model and record the obtained best-fit χ^2. A second Gaussian component is then added. In real data the detected lines appear to cluster at specific energies, and so we analysed the energy bands 4–6 keV, 6–8 keV, and 8–10 keV separately in simulated spectra. In particular, the fitted line energy is forced to vary within each of these intervals, and its width is free to vary in the range 0.01–0.5 keV. Emission and absorption features are looked for separately. To adopt a conservative approach, for each cluster of features we finally counted how many of the 1000 trials show a $\Delta\chi^2$ higher than the lowest value found in the actual data. This does automatically translate into a robust estimate of the significance of each of the detected lines. Results are shown in Table 2.

We find that both emission and absorption lines do not reach a high significance in the unobscured dataset and that they tend overall to be more significant during the obscured phase. We also find that the flux state does not seem to have a direct effect on the significance of the features. If we take into account their occurrences and calculate the binomial probability, their significance increases significantly, as shown in Table 2, where the most significant groups of features are identified with the letters A–E in the last column. The global probability that the absorption lines detected in the 6–8 keV range are not fluctuations is $\gtrsim 4\sigma$ for both source states (C, E). As for the emission lines, their estimated significance is $\gtrsim 3\sigma$ in the 4–6 keV range in all the observations (A, D), and 4σ in the 6–8 keV band during the unobscured state (B).

The transient or variable nature of the detected features is naturally inferred from the fact that they are detected only in a fraction of our time-resolved spectra.

4. Residual maps

The blind search can accurately detect features in each time bin and provides information about their possible repeated appearances at different times during the whole observations. However, it is not straightforward to understand the evolution of such features in time simply from the blind search results: an easy way to trace this evolution is to represent these features in a time–energy plane. This approach was first introduced by Iwasawa et al. (2004) and later used in several studies (e.g. Turner et al. 2006; Tombesi et al. 2007; De Marco et al. 2009; Nardini et al. 2016; Marinucci et al. 2020). As we study the presence of emission and absorption features simultaneously, we decided to visualise them together (hence the passage from *excess* to *residual* maps in the denomination).

Table 2. Significance of detected variable features.

Energy	$\Delta\chi^2$ σ_{single} (1)	MC σ_{single} (2)			σ_{group} (3)	
		Low	Mid	High		
keV	%	%	%	%	%	
Unobscured						
Emission						
4–6	91	94	92	92	99.3	A
6–8	91	94	93	93	>99.9	B
8–10	91	92	90	91	91.0	
Absorption						
4–6	92	90	91	88	87.0	
6–8	91	90	88	89	99.9	C
8–10	90	87	83	80	91.0	
Obscured						
Emission						
4–6	95	97	96	96	>99.9	D
6–8	96	99	99	98	99.0	
8–10	94	96	96	95	65.0	
Absorption						
4–6	97	97	96	97	93.0	
6–8	92	91	93	92	>99.9	E
8–10	96	96	95	95	74.0	

Notes. (1) Significance of single features calculated from the $\Delta\chi^2$ for 3 Δd.o.f. measured after the addition of a Gaussian line in emission or absorption; (2) significance of single features from MonteCarlo simulations (Low/Mid/High refer to the different selected flux levels, defined in Sect. 3.4); (3) global significance of detected features (i.e. calculated from a binomial distribution, and assuming the total number of spectra in each state as the number of trials, the number of detections obtained via the blind search as the number of successes, and the mean value from MC simulations as the success probability for each trial). The letters A–E refer to the groups of features with a significance $> 3\sigma$, as indicated in Sect. 3.4 and displayed in Fig. 5. Their nature is discussed in Sect. 5.

In order to visualise the data uniformly, we first have to choose an energy resolution for the maps. To have sufficient statistics, we impose a minimum of 20 photons in each $\Delta t \cdot \Delta E$ pixel. Having already selected $\Delta t = 5$ ks (see Sect. 3), we can adopt $\Delta E = 100$ eV, which is approximately equal to the EPIC pn energy resolution at high energies and allows us to collect more than 20 photons per time–energy pixel at all times, except for energies higher than 9 keV in the first half of O1 (where the flux is at its minimum, as shown in Fig. 1). However, with the blind search we already found that we are not able to detect significant features in this range for the obscured dataset, and therefore we decided to limit our analysis to the data below 9 keV for the RM analysis.

Figure 6 shows the RM produced by applying the baseline model described in Sect. 3.1 fitted in the total energy range. This procedure is significantly different from what is usually done in excess maps (e.g. Iwasawa et al. 2004; De Marco et al. 2009), where the continuum is typically modelled using only narrow energy bands of the spectrum where no major discrete features are expected to be observed (see Appendix A). However, for the blind search, we find that oversimplification of the modelling and/or fitting may also introduce strong systematic errors in the production of the maps (see e.g. the differences between the maps shown in Fig. 6 and in Fig. A.1).

From visual inspection of the RM, it is possible to see that the features detected in Sect. 3 (and labeled with letters A–E in Table 2) are also present in the maps, and evidently exhibit intensity variability on short timescales probed by the RM. Nevertheless, we do not find any clear macro pattern of variability.

The most evident features in the RM are of course those that are most conspicuous in the histograms in Fig. 5. The recurrent absorption feature detected via the blind search is clearly recognisable as a blue stripe at ~6.5 keV in the unobscured datasets (C), with a varying intensity on short (~10 ks) timescales. This absorption line gets wider and shifted in energy up to ~6.7–6.9 keV in the obscured dataset (E). It is interesting to see that, in the RM, this feature seems to appear far more often than in the histograms, where it reaches a maximum frequency of ~25%: this is because in the blind search we set the detection threshold to 90%, whereas the maps show all the residuals with $|\Delta\chi| > 1$, which corresponds to a lower significance of approximately 68%.

The emission features related to the neutral Fe Kβ and ionised Fe Kα are visible in the 2000 and 2001 observations as an irregular sequence of shallow red spots around ~7 keV (B). The recurrent emission features in the lower energy band (4–6 keV) also appear shallow and irregularly distributed in the unobscured dataset (A), while in the obscured dataset they are mostly clustered above 5 keV (D), as especially clear in O1. These results are discussed in Sect. 5.

Fe Kα line residuals

The RMs shown in Fig. 6 provide information about all possible lines in the 4–10 keV band except for the narrow component of the Fe Kα, as it is fitted in each spectrum, and so the residuals are null by default. Even though its variations in energy, EW, and width are already shown in Figs. 2 and 3, it would still be interesting to see them along with the other features in order to highlight possible relations. We therefore produced a new set of RMs, where we fitted the baseline model described in Sect. 3.1, froze all the parameters of the absorber and of the power law at their best-fit values, removed the line component, and then finally plotted the $\Delta\chi$. These RMs are shown in Fig. 7. The strong emission feature at ~6.4 keV is always present, but the darker and lighter spots seem to indicate some variability. Given the results obtained from the fits of our baseline model (Sect. 3.1), the observed variations in the RM can be ascribed to a combination of the variations of EW and width of the Fe Kα emission line (Fig. 2, bottom panel; Fig. 3). The possible origin of this behaviour is discussed in Sect. 5.2.

5. Discussion

In this study we searched for and identified absorption and emission features between 4 and 10 keV that are variable on short timescales in the Seyfert galaxy NGC 3783. We studied archival *XMM-Newton* observations which caught the source in two different states: one unobscured and one obscured state (as previously found by M17). This allowed us to investigate how these features change between the two states.

Features in emission. As displayed in the top left panel of Fig. 5B, about 15% of the spectra during the unobscured epochs (2000/2001) show the presence of emission features with a significance ≤90% around 7 keV. This corresponds to a global statistical significance of the detections of ~4σ (Table 2). Conversely, during the obscured epochs, the number of detections and their significance drops: we observe only one feature, detected at a significance of $< 3\sigma$. This cluster of emission lines

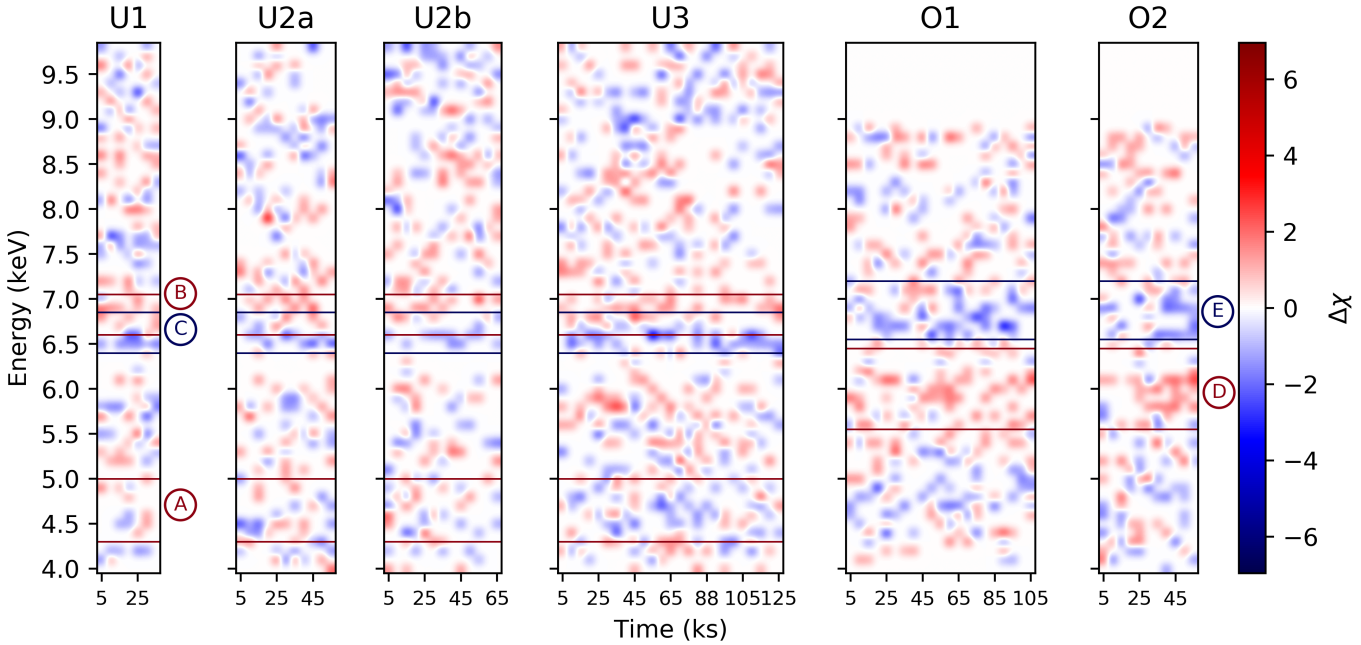

Fig. 6. Residual maps produced with the baseline model `pcfabs` × `(power law + gauss)`. The time bin size is 5 ks, while the energy resolution is 0.1 keV. Each pixel shows the value of $\Delta\chi$ (i.e. residual/data error, shown in red for the positive and in blue for the negative residuals) to give an estimate of the significance, even though the RM are meant to be used here as a qualitative way to identify patterns rather than a tool to estimate the significance of each feature. A Gaussian interpolation is applied to the pixels to highlight the features and facilitate the identification of possible patterns. The area at E >9 keV of both O1 and O2 are purposefully left blank as the threshold of 20 photons per pixel is not met because of the low flux (see Sect. 4). The horizontal lines highlight the energy bands of the most significant groups of features indicated in Fig. 5 and Table 2.

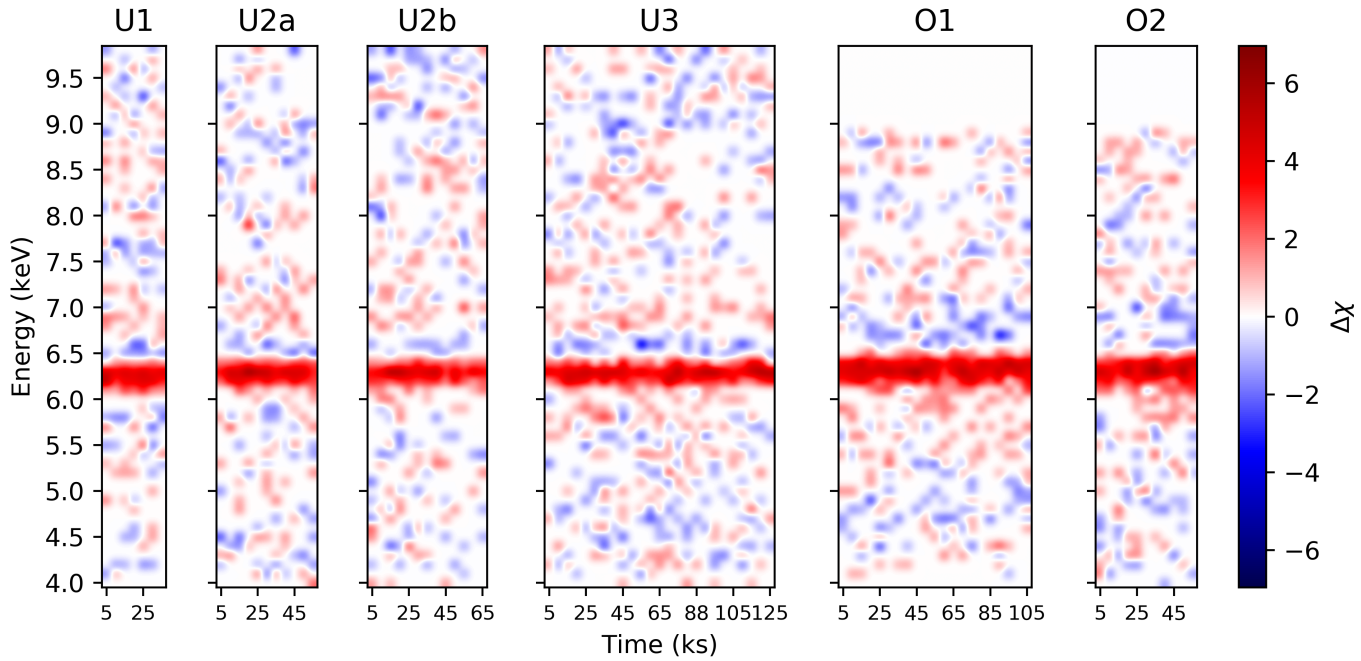

Fig. 7. Residual maps including the narrow Fe Kα component, produced as described in Sect. 4. These residuals are produced by fixing the baseline model at its best-fit values for each spectrum and then removing the Gaussian component.

in the unobscured epoch can be identified as either the neutral Fe Kβ line or an additional ionised Fe component found at ~6.9–7 keV. This identification is supported by the ratio between the residuals at ~7 keV and those at ~6.4 keV, which is about a factor three larger than what we would expect in the case of a pure Fe Kβ (~1/9) (Molendi et al. 2003). The additional contribution to the emission features at ~7 keV may come from the same ionised medium producing the absorption features. The same conclusion is given in R04. This excess is far less visible, if not absent, in the obscured dataset, as we would expect from the results of M17, who suggested that a juxtaposition with a Fe XXVI Lyα absorption line cancels out the emission feature.

The other notable cluster of emission features (though individually less significant) is seen in the obscured observations

at 5–6 keV (marked 'A' in the bottom left panel of Fig. 5) and is clearly visible in the corresponding RM (see Fig. 6). This is detected to be more variable and sporadic in the 2000 and 2001 dataset (D). The nature of these features is discussed in Sect. 5.1. The U3 data were previously analysed using the excess map technique by Tombesi et al. (2007) with a different fitting procedure (described below). These latter authors report variability and modulation of a putative red and relativistically broadened wing of the Fe K line. In their scenario, the modulation was possibly due to the formation of spiralling arms within the accretion flow. However, it is worth noting that the presence of this broad feature is not strongly supported by the analysis of the time-averaged spectrum (R04). The recurrent, redshifted feature reported in Tombesi et al. (2007) appears less prominent in our RM. This is probably due to the difference in the assumed baseline model (we assume a partial covering model for the continuum rather than a totally covering one). Moreover, when fitting the continuum, we include a narrow Fe Kα line in the model rather than excluding the energy range where it contributes the most. More details on the comparison between our results and those reported in Tombesi et al. (2007) are reported in Appendix A.

Features in absorption. The most recurrent features measured in almost 25% of all the spectra are seen in absorption between 6.7 and 6.9 keV (C and E in Fig. 5). This absorption component is also clearly visible in the RM (see Fig. 6). This is in agreement with results of R04 and M17. We also confirm that the feature's energy shifted by ~200 eV, from ~6.7 to ~6.9 keV, between the unobscured and obscured datasets (see Fig. 5). Taking into account the calibration problems highlighted in Sect. 3.2, the net energy shift of the absorption line is more likely of ~150 eV. The absorption line at 6.7 keV is observed throughout all the unobscured observations, which span a period of about one year. Nonetheless, R04 reported a change in the EW between U2 and U3. However, it is worth noting that their analysis is most probably more sensitive to slight variations of the average values, while our analysis is more focused on searching for variability on shorter timescales. Interestingly, we confirm the absence of ultra-fast outflows in this source (Tombesi et al. 2010). The results of the blind search in the energy band 8–10 keV are in fact consistent with what is expected for pure casual events (see Table 2).

5.1. Possible Fe Kα broadening during O1 and O2

To explain the origin of the group of emission features detected at $\leq 4\sigma$ in the obscured epoch in the 5–6 keV energy range (bottom-left panel of Fig. 5) and clearly visible in the corresponding RM (last two panels of Fig. 6), we propose two different scenarios. The first ascribes these features to the presence of the absorber. It may be an effect of the oversimplification of the fitted continuum model, meaning that ignoring the absorption lines and absorption edges due to the presence of an ionised absorber alters the whole continuum, occasionally resulting in excess emission redward of the Fe Kα line. Another possibility in the same scenario is that the bump is produced by variations in the partial covering fraction happening on shorter timescales than our time resolution (Iso et al. 2016). This scenario is furthermore supported by the fact that in the unobscured epoch, where the absorber has a lower column density and is less ionised (R04), the features are detected at a lower significance and at lower energies (top left panel of Fig. 5).

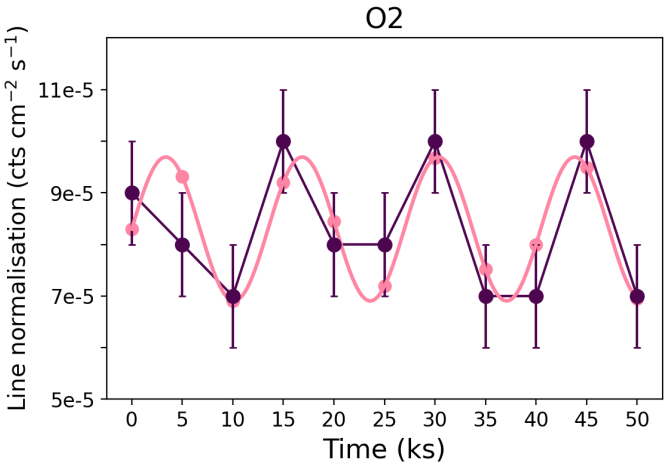

Fig. 8. Tentative fitting of a sinusoid to the variations of the normalisation of the Fe Kα.

The other scenario is that these features are real, and associated with a relativistic wing of the neutral Fe Kα line. To explore this option, we tested a relativistic model on the emission line detected at 6 keV in the twelfth 5 ks spectrum O1, which we use as a test because of its significant broadening of $\sigma = 260^{+130}_{-120}$ eV (Fig. 3). We added a `laor` component (Laor 1991) to our baseline model, which already accounts for the narrow Fe Kα. The outer radius and emissivity index are unconstrained, and so they are fixed to their default values of $400 R_g$ and 3, respectively. The excess is well reproduced ($\Delta\chi^2 = 18.3$ for 3 Δd.o.f.) by a signal emitted from $R_{in} = 99 \pm 52\ R_g$. At such a distance, the Keplerian velocity is ~30 000 km s^{-1}, corresponding to a full width at half maximum (FWHM) of ~0.64 keV for the neutral Fe Kα line at 6.4 keV. Thus, we do not expect to see much significant emission associated with it below ~6 keV, where we indeed detect the majority of emission lines (group D, bottom-left panel Fig. 5). If those features were real, they could be emitted from the base of the obscuring wind, as could be expected following the models in Dehghanian et al. (2020).

5.2. Fe Kα modulation in O2

In the residual maps of the latest observation (O2) (Fig. 7) there are four quite evident peaks in the principal Fe Kα line component. It is to be noted that their presence does not show a correlation with the 4–10 keV light curve (last panel in Fig. 1), and so the line is not simply following an intrinsic continuum variation. The normalisation of the narrow Fe Kα line, as obtained from time-resolved spectral fitting of O2, is plotted in Fig. 8. This is tentatively fit with a sinusoidal function. The fit yields $\chi^2 = 5.3$ for 8 d.o.f. (10 data-points and 2 free parameters, period and normalisation). This corresponds to a significance of 90%, and therefore does not support the detection of a modulation. However, it is worth noting that even if a modulation is indeed present, the small number of sampled variability cycles (~4) would significantly reduce the significance of the signal.

The sinusoidal fit yields a best-fit value of 13 ± 8 ks for the putative period. This would correspond to a Keplerian orbit at ~6 Rg. At such small distances, we would expect prominent relativistic effects on the Fe Kα line, which are not observed. Therefore, we conclude that the observed variations are most likely not associated with a modulation of the Fe Kα. Interestingly, the intensity of the narrow Fe Kα line seems to decrease

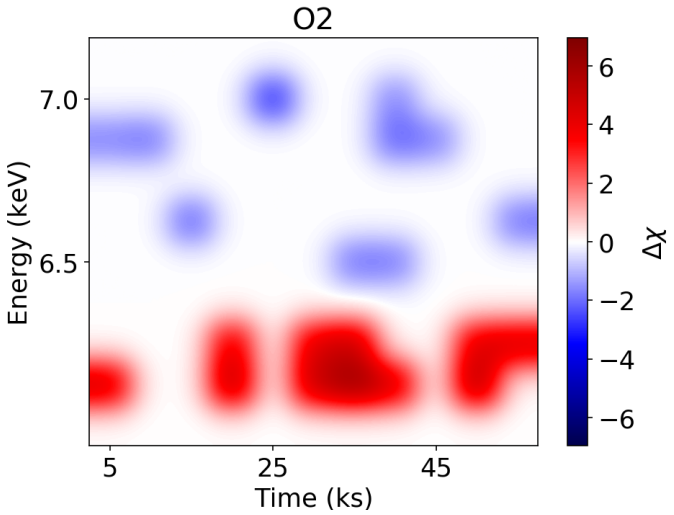

Fig. 9. Residual map of O2 where we set a higher threshold in terms of $\Delta\chi$ to qualitatively highlight the possible link between the peaks of the Fe Kα emission line (in red) and the most intense absorption dips (in blue).

simultaneously with the appearance of the absorption features at 6.7–6.9 keV, as highlighted in Fig. 9, suggesting a relation between the two.

In M17, the absorption features are ascribed to a highly ionised ($\log\xi \cong 3.8$), clumpy medium outflowing at a few thousand km s^{-1} in the broad line region. This high-ionisation component is likely associated and spatially coexistent with the obscurer producing the eclipsing event, which has a lower ionisation parameter of $\log\xi \cong 1.8$. A gas with this value of ξ could actually produce resonant absorption lines at energies consistent with the Fe Kα for ionised species from Fe X up to Fe XX (Kallman et al. 2004). In this case, the dips observed in the emission line would correspond to a partial absorption at that energy. This explanation is similar to that reported in M17 for the disappearance of the Fe Kβ emission line; the main difference is that in the case of the Fe Kα line the emission feature is not completely suppressed because of its intrinsically higher normalisation. In this scenario, we can use the duration of the dips (and the absorption features at higher energy) to constrain the size of the clumps of the obscurer. If each clump has a large opacity, we can assume an 'on/off' effect due to their passage through the line of sight. Using the distance and velocity values found in M17 for the obscurer, ∼7−10 light days from the X-ray source (few 10^3 R_g), with an orbital velocity of ∼3500−4200 km s^{-1}, and considering the duration of the dips to be from 5 ks to 10 ks, we can estimate the clumps extent to be in the range $\sim 1.7–4.2 \times 10^{13}$ cm.

While the peaks in O2 are the most evident, Fig. 7 shows that the intensity of the neutral Fe Kα emission line varies also in other observations. For O1 we can assume that the lower ionisation component is the same as in O2 (M17), and since the Fe Kα line dips have the same duration of 5–10 ks we obtain the same results for the clumps sizes.

In the unobscured epoch, R04 reports the presence of three different absorbing components at different ionisation levels. Among them, the medium with $N_{\rm H} \cong 4.4 \times 10^{22}$cm^{-2} and $\log\xi \cong 3$ can possibly absorb part of the neutral Fe Kα emission line. The entity of this absorption is actually consistent with the variations we measure in the normalisation of the line (a few percents of its value); however, it should be noted that this quantity is also of the same order of magnitude as the error on the parameter. Nevertheless, if take the variations to be real, we measure dips with a duration of between 5 ks and 20 ks. With a distance of $\sim 2 \times 10^{17}$ cm (R04), assuming a Keplerian orbit, we find the size of the clouds to be in the range of $0.7–2.8 \times 10^{11}$ cm. The dimensions of the clouds in both epochs are consistent with those found in the broad line region of NGC 1365 by Risaliti et al. (2009).

6. Conclusions

In this paper, we present a time-resolved spectral analysis of all *XMM-Newton* observations (exposure ≥10 ks) of NGC 3783. We first performed a blind search to detect any significant feature in emission or absorption and then produced residual maps to trace their evolution over time and energy, searching for variable structures that might be indicative of motions or changes in the physical state of the accreting and/or outflowing gas near the BH. Running the blind search and then producing the residual maps, we examined both positive and negative deviations found in the 4–10 keV energy band. Our approach slightly differs from those of previous works, as these latter mostly focused on studying only excess emission features and not absorption ones (e.g. Turner et al. 2006; Tombesi et al. 2007; De Marco et al. 2009; Nardini et al. 2016; Marinucci et al. 2020).

This study is complementary to the work presented in DM20, who focused on studying the soft X-ray band variability properties of the source, and to that of Tombesi et al. (2007), who characterised the variability of emission features in the unobscured dataset.

In this study, we find that NGC 3783 5 ks spectra show discrete features detected at ≤90% (Fig. 5) at different times, both in emission and in absorption, and the distributions in energy of these features change between the datasets from the two different states. In particular, all detections show a higher significance during the obscured phase than in the unobscured one and are not correlated with variations in flux. Furthermore, we observe that some of the lines appear multiple times at the same energies, reaching a global significance higher than 3σ:

- In the 4–6 keV energy band, we detect clusters of emission features in both our datasets, with a higher significance in the obscured one, whose presence we link to complex effects of the absorption mediums.
- The spectra from the unobscured epoch present an emission feature ascribable to a blend of Fe neutral Kβ and ionised Fe Kα.
- Absorption features are detected at ∼6.6 keV in the unobscured dataset and at ∼6.7−6.9 in the obscured one, produced by two distinct absorbers.

In the residual maps, we do not find any particular pattern or evolution in most of the data, except for O2 where we identify a possible modulation in the neutral Fe Kα signal that seems to be linked to variations in the recurrent absorption feature at slightly higher energies: we interpret this as an effect of the clumpiness of the absorber medium and infer the dimensions of the clumps.

The described analysis and the methodology used in this work can be extended to further bright Seyfert 1 galaxies with long and multiple *XMM-Newton* observations, and provide significant potential for use with data from next-generation X-ray instruments such as those on board the ESA mission *Athena* (Nandra et al. 2013).

Acknowledgements. We thank the anonymous referee for her/his constructive comments. This work is based on observations obtained with *XMM-Newton*, an ESA science mission with instruments and contributions directly funded by

ESA Member States and NASA. Partial support to this work was provided by the European Union Horizon 2020 Programme under the AHEAD2020 project (grant agreement number 871158). We acknowledge financial support from ASI under grants ASI-INAF I/037/12/0 and n. 2017-14-H.O, and from the grant PRIN MIUR contract no. 2017PH3WAT ("Black Hole winds and the Baryon Life Cycle of Galaxies: the stone-guest at the galaxy evolution supper"). D.C. thanks A.P. and T.S. B.D.M. acknowledges support via Ramón y Cajal Fellowship RYC2018-025950-I. P.O.P. acknowledges financial support from the High Energy National Programme (PNHE) of CNRS and from the french spatial agency CNES. E.B. was supported by a Center of Excellence of The Israel Science Foundation (grant No. 2752/19). SRON is supported financially by NWO, the Netherlands Organization for Scientific Research.

References

Arévalo, P., & Uttley, P. 2006, MNRAS, 367, 801
Arnaud, K. A. 1996, in Astronomical Data Analysis Software and Systems V, eds. G. H. Jacoby, & J. Barnes, ASP Conf. Ser., 101, 17
Bardeen, J. M., Press, W. H., & Teukolsky, S. A. 1972, ApJ, 178, 347
Barret, D., Lam Trong, T., den Herder, J. W., et al. 2018, in Space Telescopes and Instrumentation 2018: Ultraviolet to Gamma Ray, eds. J. W. A. den Herder, S. Nikzad, & K. Nakazawa, SPIE Conf. Ser., 10699, 106991G
Blustin, A. J., Page, M. J., Fuerst, S. V., Branduardi-Raymont, G., & Ashton, C. E. 2005, A&A, 431, 111
Cappi, M., De Marco, B., Ponti, G., et al. 2016, A&A, 592, A27
Dadina, M., Cappi, M., Malaguti, G., Ponti, G., & de Rosa, A. 2005, A&A, 442, 461
Dehghanian, M., Ferland, G. J., Kriss, G. A., et al. 2020, ApJ, 898, 141
De Marco, B., Iwasawa, K., Cappi, M., et al. 2009, A&A, 507, 159
De Marco, B., Adhikari, T. P., Ponti, G., et al. 2020, A&A, 634, A65
Fabian, A. C., Iwasawa, K., Reynolds, C. S., & Young, A. J. 2000, PASP, 112, 1145
Gofford, J., Reeves, J. N., Tombesi, F., et al. 2013, MNRAS, 430, 60
Iso, N., Ebisawa, K., Sameshima, H., et al. 2016, PASJ, 68, S27
Iwasawa, K., Miniutti, G., & Fabian, A. C. 2004, MNRAS, 355, 1073
Kaastra, J. S., Kriss, G. A., Cappi, M., et al. 2014, Science, 345, 64
Kaastra, J. S., Mehdipour, M., Behar, E., et al. 2018, A&A, 619, A112
Kallman, T. R., Palmeri, P., Bautista, M. A., Mendoza, C., & Krolik, J. H. 2004, ApJS, 155, 675
Kotov, O., Churazov, E., & Gilfanov, M. 2001, MNRAS, 327, 799
Laha, S., Guainazzi, M., Dewangan, G. C., Chakravorty, S., & Kembhavi, A. K. 2014, MNRAS, 441, 2613
Laor, A. 1991, ApJ, 376, 90
Longinotti, A. L., Bianchi, S., Ballo, L., de La Calle, I., & Guainazzi, M. 2009, MNRAS, 394, L1
Mao, J., Mehdipour, M., Kaastra, J. S., et al. 2019, A&A, 621, A99
Marinucci, A., Bianchi, S., Braito, V., et al. 2020, MNRAS, 496, 3412
McKernan, B., Yaqoob, T., & Reynolds, C. S. 2007, MNRAS, 379, 1359
Mehdipour, M., Kaastra, J. S., Kriss, G. A., et al. 2015, A&A, 575, A22
Mehdipour, M., Kaastra, J. S., Kriss, G. A., et al. 2017, A&A, 607, A28
Miniutti, G., & Fabian, A. C. 2004, MNRAS, 349, 1435
Molendi, S., Bianchi, S., & Matt, G. 2003, MNRAS, 343, L1
Mushotzky, R. F., Done, C., & Pounds, K. A. 1993, ARA&A, 31, 717
Nandra, K., Barret, D., Barcons, X., et al. 2013, ArXiv e-prints [arXiv:1306.2307]
Nardini, E., Porquet, D., Reeves, J. N., et al. 2016, ApJ, 832, 45
Padovani, P., Alexander, D. M., Assef, R. J., et al. 2017, A&ARv, 25, 2
Peterson, B. M., Ferrarese, L., Gilbert, K. M., et al. 2004, ApJ, 613, 682
Piconcelli, E., Jimenez-Bailón, E., Guainazzi, M., et al. 2005, A&A, 432, 15
Ponti, G., Cappi, M., Costantini, E., et al. 2013, A&A, 549, A72
Pounds, K. A., Reeves, J. N., King, A. R., et al. 2003, MNRAS, 345, 705
Protassov, R., van Dyk, D. A., Connors, A., Kashyap, V. L., & Siemiginowska, A. 2002, ApJ, 571, 545
Reeves, J. N., O'Brien, P. T., & Ward, M. J. 2003, ApJ, 593, L65
Reeves, J. N., Nandra, K., George, I. M., et al. 2004, ApJ, 602, 648
Reeves, J. N., Braito, V., Gofford, J., et al. 2014, ApJ, 780, 45
Risaliti, G., Miniutti, G., Elvis, M., et al. 2009, ApJ, 696, 160
Theureau, G., Bottinelli, L., Coudreau-Durand, N., et al. 1998, A&AS, 130, 333
Tombesi, F., de Marco, B., Iwasawa, K., et al. 2007, A&A, 467, 1057
Tombesi, F., Cappi, M., Reeves, J. N., et al. 2010, A&A, 521, A57
Turner, T. J., Miller, L., George, I. M., & Reeves, J. N. 2006, A&A, 445, 59
Turner, T. J., Miller, L., Kraemer, S. B., Reeves, J. N., & Pounds, K. A. 2009, ApJ, 698, 99
Urry, C. M., & Padovani, P. 1995, PASP, 107, 803
Vaughan, S., & Uttley, P. 2008, MNRAS, 390, 421
Webb, N. A., Coriat, M., Traulsen, I., et al. 2020, A&A, 641, A136
Yaqoob, T., Reeves, J. N., Markowitz, A., Serlemitsos, P. J., & Padmanabhan, U. 2005, ApJ, 627, 156
Zoghbi, A., Miller, J. M., & Cackett, E. 2019, ApJ, 884, 26

Appendix A: Continuum fitting in residual maps

As stated in Sect. 5, our residual maps were produced in a slightly different fashion from those described by Tombesi et al. (2007). Aside from the major step of employing all of the residuals, positive and negative, and not only the positive ones, we used a different fitting procedure.

To study the emission features, Tombesi et al. (2007) modelled the continuum as a power law plus a cold absorption component fixed to be equal to the value measured in analysing the average spectrum. They then fitted the continuum considering the 4–5 keV and 7–9 keV band to avoid the Fe Kα line. Applying the exact same procedure we produced the RMs shown in the top panel of Fig. A.1.

As we were interested in following the variations of the absorptions features produced indeed by the absorber, we produced another set of RMs with the same fitting band and model, this time leaving the column density free to vary in each spectrum. These are displayed in the bottom panel of Fig. A.1.

While these two sets of maps do not show significant divergence from one to the other, as indeed predicted by Tombesi et al. (2007), the difference between them and those we present in Fig. 7 is quite evident. The absorption features we find at ~6.6–6.9 keV are only marginally present in the RM in Fig. A.1. Instead, the excess at energies below the Fe Kα line appear to be far more intense and, in particular, in U3 we find the strong feature discussed by Tombesi et al. (2007). It should be noted that the normalisation (colour) of the residual maps is the same for all sets.

The first difference between the production of the maps shown in Fig. 6 and those in Fig. A.1 is the energy band used to fit the model. The use of the complete 4–10 keV range, without excluding the Fe Kα band, allows for a better anchorage of the continuum, and this could be at the basis of the divergence of the sets of maps. We then analysed the continuum parameters: in the top left panel of Fig. A.2 we plot the best-fit parameters for the absorber column density and the power-law photon index. To quantify the relation among them, we calculated the Pearson correlation coefficient ρ for the two epochs, and obtained $\rho_U = 0.78$ and $\rho_O = 0.88$, both corresponding to a correlation probability higher than 5σ. This degeneracy between these two parameters disappears when using the partial covering baseline model, described in Sect. 3.1. Its best fit parameters are plotted in the bottom panel of Fig. A.2, and the correlation probability calculated for these data drops at 21% for the unobscured epoch ($\rho_U = -0.04$) and 17% for the obscured one ($\rho_O = 0.04$). On the one hand, it is worth considering that we are in any case dealing, by construction, with limited statistics. This means that our approach is also prone to introducing some systematic errors, as seen in the bottom panels of Fig. A.2. This is somewhat inevitable given the experimental condition that we are using. On the other hand, we already knew that our baseline model provides a limited description of the complex absorption that is known to occur in NGC 3783 (Mehdipour et al. 2017; Mao et al. 2019). A detailed investigation of the characteristics of the various ionised absorbers that have been previously reported in the literature is far beyond our present scope; we want to stress here that at least part of the excesses recorded between 5 and 6 keV are possibly explained by the simplified absorption scheme used in producing the RMs. A significant step forward in time-resolved spectral studies will be possible with X-ray telescopes with larger effective areas, which would allow us to probe short timescales (i.e. using short time slices) without losing energy resolution. Specifically, the X-IFU on board Athena (Nandra et al. 2013; Barret et al. 2018) will in the foreseeable future provide a major advance in the research field described in this paper.

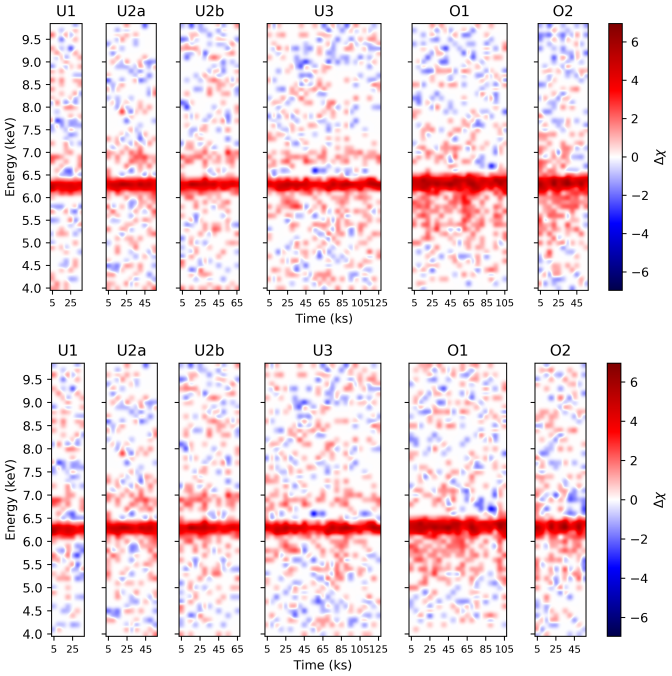

Fig. A.1. RMs produced using a power law plus total covering cold absorption fitted only in the 4–5 keV and 7–10 keV energy bands, following the indications of Tombesi et al. (2007). The value of the column density of the absorber is fixed to the value measured in average spectra in top panel maps and free to vary in the bottom panel ones.

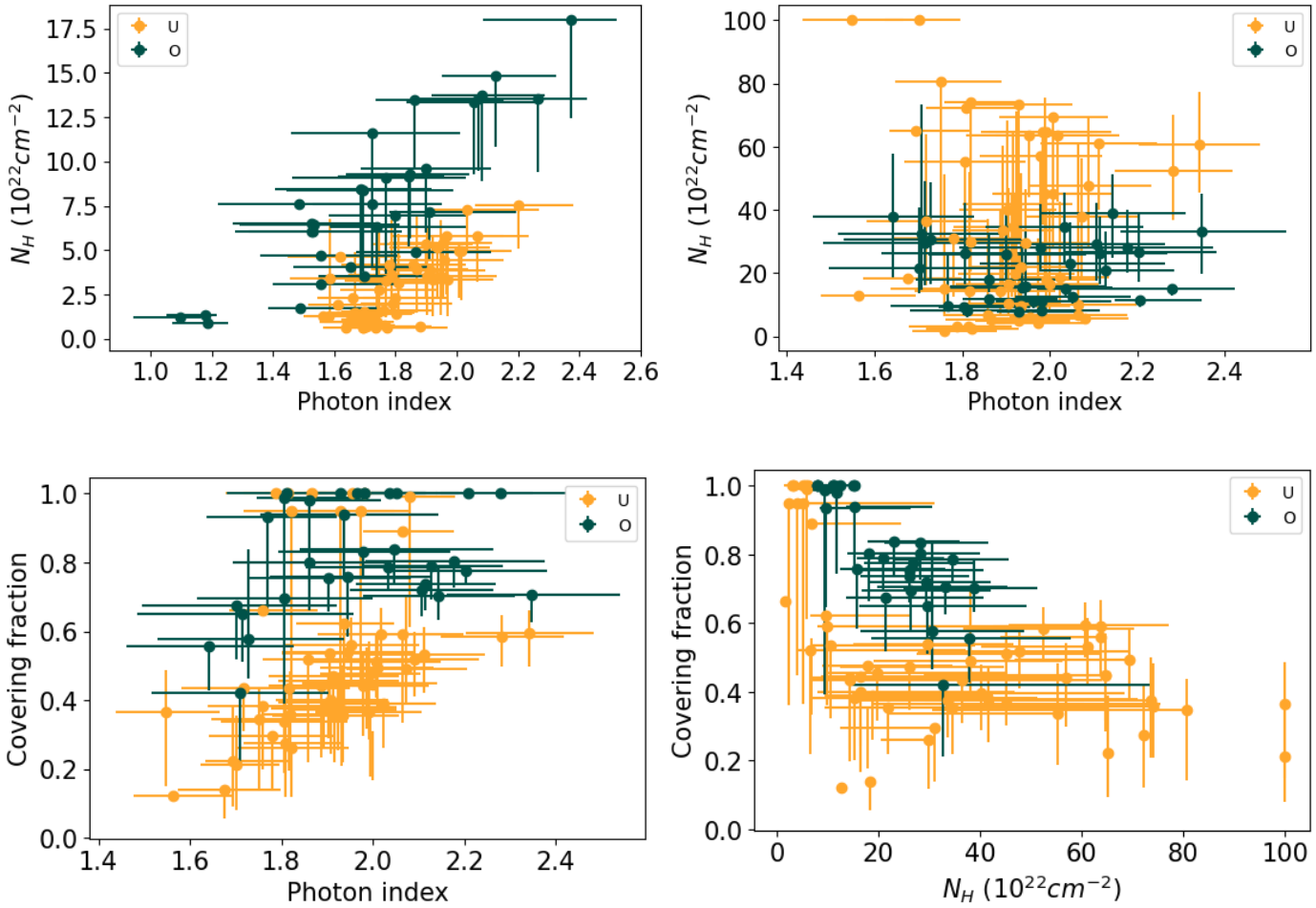

Fig. A.2. Top left panel: Column density of the total covering cold absorption vs power-law photon index, fitted only in the 4-5 keV and 7-10 keV energy bands. The correlation among the values is assessed at $\gg 5\sigma$ for both the unobscured and obscured epoch. Top right panel: Column density of the partial covering cold absorption vs power-law photon index, fitted in the 4-10 keV energy range. The degeneracy between the two parameters is not present in this case, with a correlation probability $\lesssim$20%. Bottom left panel: Covering fraction of the partial covering absorber vs power-law photon index. Bottom right panel: Covering fraction vs column density of the absorber. Data relative to unobscured and obscured epoch are reported in yellow and green respectively.